Predicting the Slowing of Stellar Differential Rotation by Instability-driven Turbulence

B. Tripathi[1] , A. J. Barker[2] , A. E. Fraser[3,4,5] , P. W. Terry[1] , and E. G. Zweibel[1,6]

[1] Department of Physics, University of Wisconsin-Madison, Madison, WI 53706, USA; btripathi@wisc.edu
[2] Department of Applied Mathematics, School of Mathematics, University of Leeds, Leeds, LS2 9JT, UK; A.J.Barker@leeds.ac.uk
[3] Department of Applied Mathematics, University of Colorado, Boulder, CO 80309, USA
[4] Department of Astrophysical and Planetary Sciences, University of Colorado, Boulder, CO 80309, USA
[5] Laboratory for Atmospheric and Space Physics, University of Colorado, Boulder, CO 80309, USA
[6] Department of Astronomy, University of Wisconsin-Madison, Madison, WI 53706, USA

Abstract

Differentially rotating stars and planets transport angular momentum (AM) internally due to turbulence at rates that have long been a challenge to predict reliably. We develop a self-consistent saturation theory, using a statistical closure approximation, for hydrodynamic turbulence driven by the axisymmetric Goldreich–Schubert–Fricke instability at the stellar equator with radial differential rotation. This instability arises when fast thermal diffusion eliminates the stabilizing effects of buoyancy forces in a system where a stabilizing entropy gradient dominates over the destabilizing AM gradient. Our turbulence closure invokes a dominant three-wave coupling between pairs of linearly unstable eigenmodes and a near-zero frequency, viscously damped eigenmode that features latitudinal jets. We derive turbulent transport rates of momentum and heat and provide them in analytic forms. Such formulae, free of tunable model parameters, are tested against direct numerical simulations; the comparison shows good agreement. They improve upon prior quasi-linear or "parasitic saturation" models containing a free parameter. Given model correspondences, we also extend this theory to heat and compositional transport for axisymmetric thermohaline-instability-driven turbulence in certain regimes.

Unified Astronomy Thesaurus concepts: Astrophysical fluid dynamics (101); Solar differential rotation (1996); Stellar rotation (1629); Stellar interiors (1606); Hydrodynamics (1963); Extrasolar gaseous giant planets (509)

1. Introduction

Instability-driven turbulence is thought to play a major role in the transport of angular momentum (AM), heat, and composition in stellar and planetary interiors (see, e.g., Garaud 2018; Aerts et al. 2019; Fuller et al. 2019; Spruit 2002), as well as in astrophysical disks (e.g., Balbus & Hawley 1998; Lesur et al. 2023). Unfortunately, rates of turbulent transport are very challenging to predict theoretically, and the lack of reliable theories has hampered our understanding of the evolution of stellar and planetary internal rotations and structures. For example, the AM redistribution in red giant stars is currently poorly understood, and their core–envelope differential rotations inferred from asteroseismology have not been adequately explained (e.g., Beck et al. 2012; Eggenberger et al. 2012; Aerts et al. 2019). The nearly solid-body rotation observed in the solar radiative interior also lacks a robust explanation (e.g., Garaud & Garaud 2008; Wood & McIntyre 2011).

Differential rotation is known to drive a variety of hydrodynamic (and hydromagnetic) instabilities. In this paper, we focus on modeling hydrodynamic instabilities of differential rotation in stellar and planetary radiative zones, and in particular on the Goldreich–Schubert–Fricke (GSF) instability[7]

---

[7] It has also been referred to as the "vertical shear instability" in accretion disks (e.g., Urpin & Brandenburg 1998; Nelson et al. 2013; Barker & Latter 2015; Latter & Papaloizou 2018) and as "inertial instability" enabled by thermal diffusion in stellar interiors (Park et al. 2020, 2021).

(Goldreich & Schubert 1967; Fricke 1968). This is a double-diffusive centrifugal instability, in which rapid thermal diffusion (relative to viscous momentum diffusion) enables instability by tempering the otherwise stabilizing effects of buoyancy forces. Prior work has studied the linear and nonlinear properties of the instability, and the turbulence it drives (Knobloch 1982; Knobloch & Spruit 1982; Korycansky 1991; Rashid et al. 2008; Barker et al. 2019, 2020; Dymott et al. 2023), but a reliable theory for the resulting turbulent transport is lacking. This means that the effects of the GSF instability on stellar rotational and chemical evolution have not been modeled in a self-consistent manner. Instead, one typically invokes unexplained "additional viscosities" or models that contain free parameters. Such tunable parameters are intended to describe the effects of turbulence on AM transport for which adequate knowledge is lacking.

A fully analytic model containing no free parameters is derived here for the GSF-instability-driven turbulence in 2.5 dimensions (2.5D), i.e., with all three components of velocity but varying spatially only in two dimensions. The predictions of our analytical model are in broad agreement with detailed numerical simulations of turbulence, driven by the axisymmetric (2.5D) GSF instability at the equator of a star with radial differential rotation. Such a model of the instability is, for certain diffusivity ratios and in 2.5D, formally and nonlinearly equivalent to the thermohaline, or salt-finger, instability that transports heat and chemical elements (Knobloch 1982; Barker et al. 2019); thus, the turbulent transport arising from axisymmetric fingering convection is also described by our theory.

The structure of this paper is as follows. In Section 2, we present our model and methods of analysis. Nonlinear mode coupling and saturation diagnostics of the instability appear in
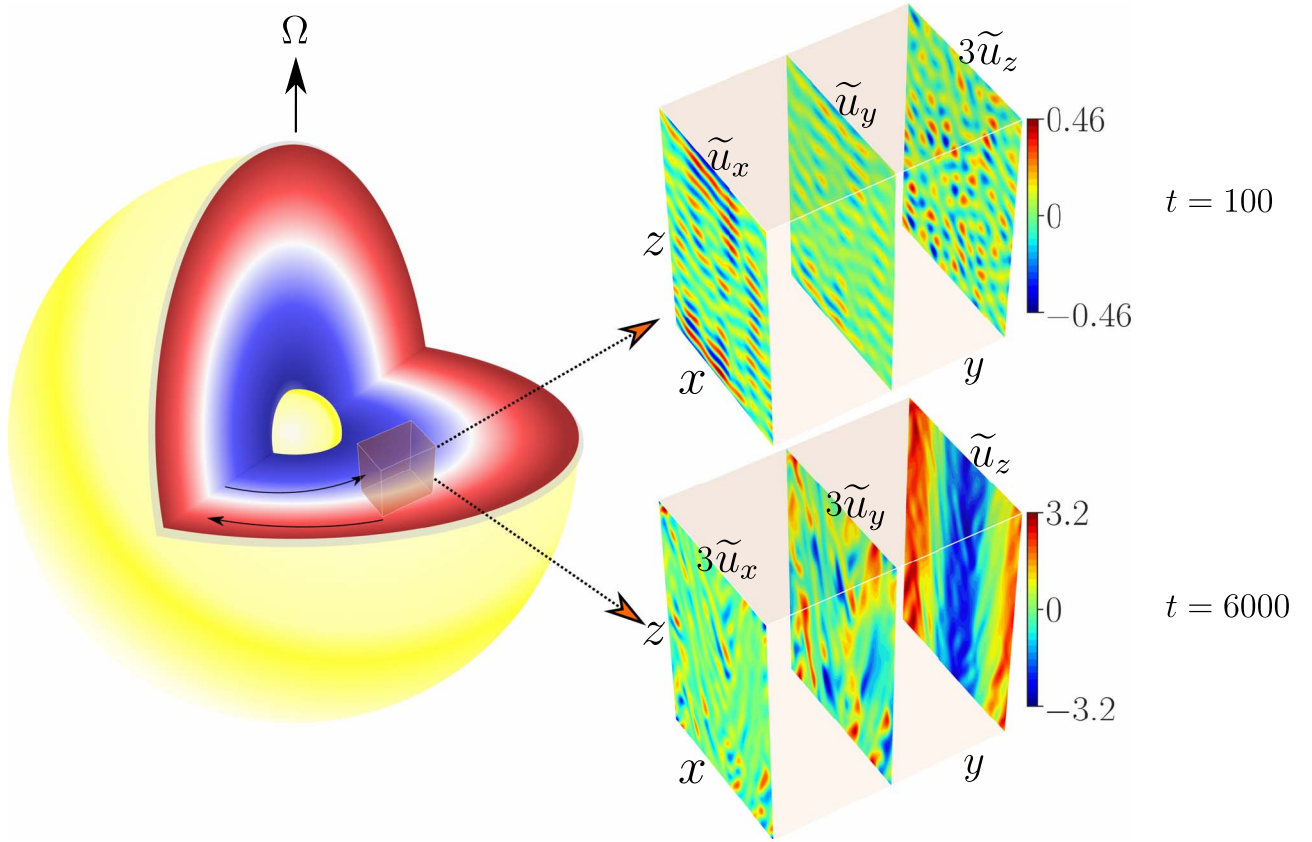
Figure 1. Left: a schematic diagram of a differentially rotating star with a radial shear, gravity, and stable stratification. Such a system subject to the GSF instability is studied using a local Cartesian model. Right: snapshots of the velocity components $\tilde{u}_x(x, z)$, $\tilde{u}_y(x, z)$, and $\tilde{u}_z(x, z)$ from the axisymmetric GSF-instability-driven turbulence; x, y, and z represent the local radial, azimuthal, and latitudinal directions, respectively. Though finger-like horizontal structures (as shown by, e.g., $\tilde{u}_x$) grow the fastest in the linear phase ($t = 100$), strong latitudinal jets $\tilde{u}_z$ are generated nonlinearly ($t = 6000$). The color bar for $t = 100$ is shared by $\tilde{u}_x$, $\tilde{u}_y$, and $3\tilde{u}_z$; the color bar for $t = 6000$ is shared by $3\tilde{u}_x$, $3\tilde{u}_y$, and $\tilde{u}_z$. The turbulent transport of AM, e.g., $\langle \tilde{u}_x \tilde{u}_y \rangle$, is predicted in this paper using a jet-coupled turbulence closure.

Section 3. Informed by such diagnostics, we present analytical formulae, without any free parameters, to model the turbulence and its transport properties in Section 4. We discuss the astrophysical implications and conclude in Section 5. Details of the closure model are provided in Appendices A, B, and C.

2. The GSF Instability and Inertial Gravity Waves

To study a basic mechanism of AM transport in a differentially rotating star, we consider a local region inside the star near its equator, where the rotation can be split into a uniform or mean part—$\mathbf{\Omega} = \Omega \hat{e}_z$, aligning with the local latitudinal axis z—and a nonuniform part due to the radial differential rotation. The latter is represented by a background linear shear flow $\mathbf{U}_0(x) = -\mathcal{S} x \hat{e}_y$, where x is the radial coordinate, y is the azimuthal coordinate, and $\mathcal{S} = -d\Omega_{\text{Shell}}(x)/d\ln x$ is the local radial shear rate, with $\Omega_{\text{Shell}}(x)$ representing the "Shellular" rotation of the simplified star. A uniform gravity field with $\mathbf{g} = -g\hat{e}_x$ is directed radially inward (Figure 1). A background radial temperature gradient ∇T_0 then stratifies the fluid density radially, with a thermal expansion coefficient α. In such a background state, any perturbations in velocity $\mathbf{u}$ and scaled temperature $\theta = \alpha g T$ evolve (Barker et al. 2019) as

$$D\mathbf{u} + \mathbf{u} \cdot \nabla \mathbf{U}_0 + 2\mathbf{\Omega} \times \mathbf{u} = -\nabla p + \theta \hat{e}_x + \nu \nabla^2 \mathbf{u}, \quad (1a)$$

$$D\theta + \mathbf{u} \cdot \nabla \Theta_0 = \kappa \nabla^2 \theta, \quad (1b)$$

$$\nabla \cdot \mathbf{u} = 0, \quad (1c)$$

$$D \equiv \partial_t + (\mathbf{u} + \mathbf{U}_0) \cdot \nabla, \quad (1d)$$

where the variables p, ν, and κ are the fluid pressure (per unit density), the kinematic viscosity, and the thermal diffusivity, respectively. We also define the Prandtl number $\text{Pr} = \nu/\kappa$. Because the GSF instability operates at length scales much smaller than a pressure scale height in stars, the local approximation is valid; in such a case, when the turbulence drives subsonic flows, the Boussinesq approximation is also appropriate (Spiegel & Veronis 1960). Assuming a uniform temperature gradient, a fluid element perturbed radially oscillates with a constant Brunt–Väisälä (buoyancy) frequency $\mathcal{N}$, where $\mathcal{N}^2 \hat{e}_x = \nabla \Theta_0 = \alpha g \nabla T_0$.

Henceforth, we nondimensionalize all variables using the characteristic rotation timescale Ω^{-1} and length scale d, with $d = (\nu\kappa/\mathcal{N}^2)^{1/4}$, which is typically similar to the wavelengths of the fastest-growing modes. Thus, $N = \mathcal{N}/\Omega$ is the dimensionless buoyancy frequency and $S = \mathcal{S}/\Omega$ is the dimensionless shear rate (Rossby number). The GSF instability occurs in low-Pr fluids whenever $r \in (0, 1)$, where $r = \text{Pr}\,(1 + N^2 \kappa_{\text{ep}}^{-2})/(\text{Pr} - 1)$, with $\kappa_{\text{ep}} = \sqrt{2(2 - S)}$ representing the dimensionless epicyclic frequency (Barker et al. 2019).

2.1. Eigenmode Analysis

A linear analysis of Equations (1a)–(1b) for axisymmetric (uniform-in-y) perturbations yields a simple matrix equation, which upon Fourier-transforming becomes $\mathbf{L}\hat{X} = \gamma \hat{X}$, where

$\hat{X} = [\hat{u}_x, \hat{u}_y, \hat{u}_z, \hat{\theta}]^{\mathrm{T}}$, with $^{\mathrm{T}}$ as the transpose operation, is the state vector of spatially Fourier-transformed components at wavevector $k = (k_x, k_z)$; the matrix L is a linear operator, whose eigenvalues are the complex-valued growth rates γ. The size of L demands four linearly independent eigenvectors. Because of the additional constraint $\nabla \cdot u = 0$, the system has only 3 degrees of freedom at any given wavenumber—$\hat{\theta}$ and two components of velocity. Hence, one eigenvector among the four eigenvectors does not satisfy $\nabla \cdot u = 0$ and is rejected. We confirm that this eigenvector is not excited within our incompressible Boussinesq simulations. One among the remaining three eigenvectors at a given wavevector becomes GSF-unstable (Re $(\gamma) > 0$, where Re denotes the real part), whenever $r \in [0, 1)$. The remaining two eigenvectors are always stable, and their eigenvalues are complex conjugates of each other whenever they satisfy Im $(\gamma) \neq 0$, where Im denotes the imaginary part; Im (γ) corresponds to the frequency of inertial gravity waves (IGWs; or gravito-inertial waves), modified by the shear flow and damped by viscous and thermal diffusion.

The GSF instability grows dominantly via axisymmetric ($\partial_y \equiv 0$) perturbations, therefore we focus upon the (x, z)-variations of the three-component velocity and temperature fields. The dispersion relation is then a simple cubic polynomial in γ (Goldreich & Schubert 1967), as

$$\gamma_\nu^2 \gamma_\kappa + \frac{\kappa_{\mathrm{ep}}^2 k_z^2}{k^2} \gamma_\kappa + \frac{N^2 k_z^2}{k^2} \gamma_\nu = 0, \qquad (2)$$

where $\gamma_\nu = \gamma + \nu k^2$ and $\gamma_\kappa = \gamma + \kappa k^2$. Equation (2) shows that on the (k_x, k_z)-plane, the growth rate exhibits strong anisotropy: fluctuations with $k_x = 0$ ("elevator modes") grow the fastest, whereas those with $k_z = 0$ are linearly stable. This observation is critical for the nonlinear saturation of the GSF instability, because the anisotropy of the linear physics, in particular the $k_z = 0$ fluctuation, can impose its anisotropy on the nonlinear energy transfer, which is otherwise isotropic; such consequential effects have been found in various systems such as 3D Kelvin–Helmholtz instability (Tripathi et al. 2023b), rotating (Waleffe 1993; Smith & Waleffe 1999) and stably stratified turbulence (Riley & Lelong 2000), and turbulence with an external magnetic field in astrophysical (Ng & Bhattacharjee 1996; Du et al. 2023) and fusion plasmas (Biskamp & Zeiler 1995; Terry 2004).

Using the complete basis provided by the eigenvectors of the linear operator L, we can decompose the arbitrary incompressible fluctuation $\hat{X}_{\mathrm{arb}}$ with $k_z \neq 0$ as $\hat{X}_{\mathrm{arb}} = \sum_{j=1}^3 \beta_j \hat{X}_j$, where β_j is the amplitude of the jth eigenvector $\hat{X}_j$; we reserve $j = 1$ for the GSF-unstable modes and $j = 2, 3$ for the IGWs that are always linearly stable in this study. More compactly, $\hat{X}_{\mathrm{arb}} = E\beta$, where β is a (column) vector of mode amplitudes and E is an eigenvector matrix, whose jth column is $\hat{X}_j$. Thus, $\beta = E^{-1}\hat{X}_{\mathrm{arb}}$.

For the $k_z = 0$ modes, E turns out to be an identity matrix, meaning that the three components of velocity, and the temperature, individually form eigenvectors. In what follows, we therefore decompose an arbitrary fluctuation with $k_z = 0$ into $\hat{X}_{\mathrm{arb}}^{\mathrm{T}} = \mathcal{X}[1, 0, 0, 0] + \mathcal{Y}[0, 1, 0, 0] + \mathcal{Z}[0, 0, 1, 0] + \Theta [0, 0, 0, 1]$, where the amplitudes of the eigenvectors are denoted by $\mathcal{X}, \mathcal{Y}, \mathcal{Z},$ and Θ. We reserve the β-notation above for the amplitudes of eigenvectors with $k_z \neq 0$.

2.2. Initial Value Problem

We perform an ensemble of direct numerical simulations of Equations (1a) and (1b), by seeding a low-amplitude solenoidal random noise to u, in a box of size $(L_x, L_z) = (100, 100)$. To obtain numerically converged results, a spatial resolution of up to 512^2 grid points is used in the pseudo-spectral solver SNOOPY (Lesur & Longaretti 2005; Barker et al. 2019).

To determine the contribution of each eigenmode in, for example, the turbulent momentum transport, we decompose the turbulent stress as: $\langle \tilde{u}_x \tilde{u}_y \rangle = \sum_{k_x, k_z} \sum_{m,n} 2 \,\mathrm{Re}\,[\beta_m \hat{u}_{x,m} \beta_n^* \hat{u}_{y,n}^*]$, where $\langle \cdot \rangle$ is an (x, z)-averaging operation; m and n are summed from 1 to 3, corresponding to three excited eigenmodes at every wavenumber k; the amplitude β_m and the x-component of the velocity $\hat{u}_{x,m}$ correspond to the mth eigenvector at k, and likewise for β_n and $\hat{u}_{y,n}$; and the operation * denotes complex conjugation. Using such a decomposition, we obtain the contribution of an unstable mode at k to the momentum transport rate, which is $2|\beta_1|^2 \,\mathrm{Re}\,[\hat{u}_{x,1}\hat{u}_{y,1}^*]$. This decomposition is performed for every wavenumber, hence allowing us to trace the evolution of transport contributions due to individual unstable modes (see Figure 2(a)).

The summed contributions of all eigenvectors from all wavenumbers reproduce, to machine precision, the total transport rates found in the simulation before performing mode decomposition, as we show in Figure 2(b). The contributions of the unstable modes are also compared across different wavenumber sums. Almost identical results are found for heat transport (not shown). The unstable modes from the linearly fastest-growing wavenumber branch $k_x = 0$ transport significantly less momentum than the other wavenumbers with $k_x \neq 0$. This is our first surprising result, and it challenges predictions of turbulent transport that rely on an unstable mode at the fastest-growing wavenumber alone (e.g., Radko & Smith 2012; Brown et al. 2013; Barker et al. 2019). This finding also instructs us to investigate nonlinear couplings between eigenmodes to understand the instability saturation mechanism.

3. Nonlinear Saturation by Coupling to Latitudinal Flow

3.1. Mode Amplitude Evolution

To analyze nonlinear mode couplings, Equations (1a)–(1b) are first spatially Fourier-transformed: $\partial_t \hat{X} = L\hat{X} + \sum_{k',k''} N(\hat{X}', \hat{X}'')$, where $\hat{X}$, $\hat{X}'$, and $\hat{X}''$ are state vectors at $k, k',$ and k'', respectively, satisfying $k = k' + k''$. Then, following Section 2.1, we substitute $\hat{X} = E\beta$, and likewise for $\hat{X}'$ and $\hat{X}''$. We multiply the obtained equation with E^{-1} and take the jth row of the resulting equation. This process yields an evolution equation for the jth eigenmode at k. Such an evolution equation for mode amplitude β_j for $k_z \neq 0$ is different from that of the mode amplitude $F \in \{\mathcal{X}, \mathcal{Y}, \mathcal{Z}, \Theta\}$ for $k_z = 0$, although both are coupled and nonlinear:

$$\partial_t \beta_j = \gamma_j \beta_j + \sum_{k',m,n} C_{jmn}^{(k,k')} \beta_m' \beta_n''$$

$$+ \sum_{\substack{k',F,n:k_z'=0 \\ F \in \{\mathcal{X}, \mathcal{Y}, \mathcal{Z}, \Theta\}}} [C_{jFn}^{(k,k')} + C_{jnF}^{(k,k'')}] F' \beta_n'', \qquad (3a)$$

$$\partial_t F = -\gamma_F F + \sum_{k',m,n:k_z=0} C_{Fmn}^{(k,k')} \beta_m' \beta_n'', \qquad (3b)$$

where γ_j is the complex-valued growth rate for the jth eigenmode with $k_z \neq 0$; the real-valued damping rate γ_F is $\gamma_{\mathcal{X}}$
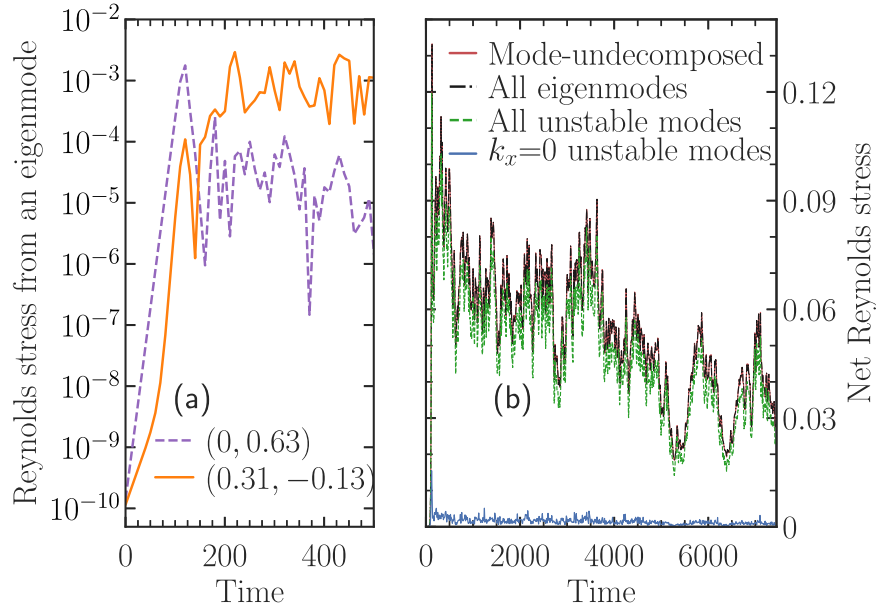
Figure 2. (a) Comparison of momentum transport (Reynolds Stress = $2|\beta_1|^2 \, \mathrm{Re} \, [\hat{u}_{x,1} \hat{u}_{y,1}^*]$) driven by an unstable mode at the linearly fastest-growing wavenumber $\boldsymbol{k} = (0, 0.63)$ and by an unstable mode at $\boldsymbol{k} = (0.31, -0.13)$, the wavenumber that has the largest contribution to the momentum transport in the nonlinear phase. (b) Eigenmode decomposition of net Reynolds stress $\langle \tilde{u}_x \tilde{u}_y \rangle$ in a nonlinear simulation of the GSF-instability-driven turbulence, showing that the transport due to mode-undecomposed fluctuations (red curve) and all mode-decomposed fluctuations (black curve) agree to machine precision. Transport is almost entirely (88%) due to the unstable modes (green curve); the sum of the fastest-growing unstable modes at $k_x = 0$, however, contributes negligibly (3%) to the transport (blue curve). The simulation parameters used are $S = 2.1$, $N^2 = 10$, and $\mathrm{Pr} = 0.01$.
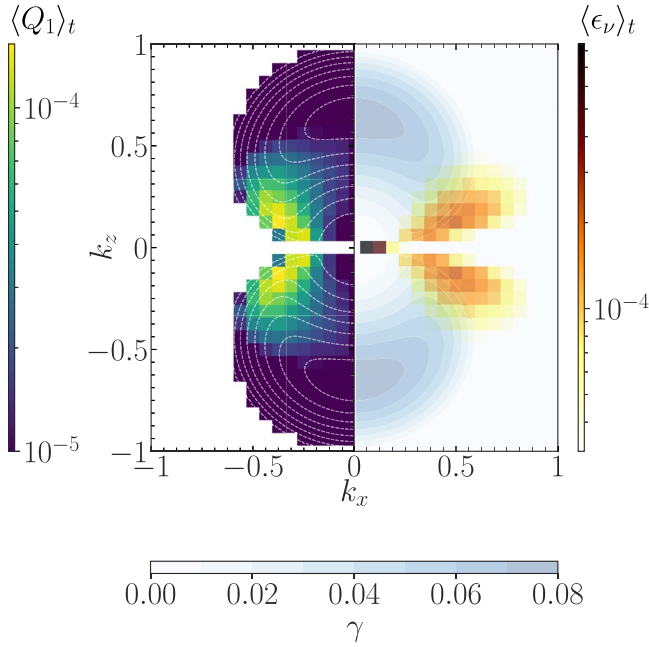

Figure 3. Spectra of linear and nonlinear saturation properties of the GSF instability. In the negative-k_x domain, the colored square boxes (yellow–green–purple) display time-averaged energy extraction rates $\langle Q_1 \rangle_t$ by unstable modes from the mean gradients in a nonlinear simulation. In the positive-k_x domain, the colored square boxes (black–red–yellow) show the time-averaged viscous dissipation rates, which are pronounced at low k_z. Over the entire (k_x, k_z)-plane, the nonsquare filled and line contours show the growth rates γ of unstable modes, with white dashed contour lines in the negative-k_x domain and bluish filled contours in the positive-k_x domain. The fastest-growing mode resides at around $\boldsymbol{k} = (0, 0.63)$. The simulation parameters are $S = 2.1$, $N^2 = 10$, and $\mathrm{Pr} = 0.01$.

when F is replaced with $\mathcal{X}$ in Equation (3b); likewise for the replacement of F with $\mathcal{Y}$, $\mathcal{Z}$, and Θ; and we note that $\gamma_{\mathcal{X}} = \gamma_{\mathcal{Y}} = \gamma_{\mathcal{Z}} = \nu k_x^2$ and $\gamma_{\Theta} = \kappa k_x^2$. The nonlinear coupling

coefficient, for example, $C_{jmn}^{(\boldsymbol{k}, \boldsymbol{k}')}$, measures the overlap of eigenmodes m with $\boldsymbol{k}'$, n with $\boldsymbol{k}''$, and j with $\boldsymbol{k}$. Such a mode-coupling coefficient is found by applying $\boldsymbol{E}^{-1}$ to the (column) vector of $\boldsymbol{N}(\hat{\boldsymbol{X}}_m', \hat{\boldsymbol{X}}_n'')$, a process that incorporates all the nonlinearities of the system, thus making $C_{jmn}^{(\boldsymbol{k}, \boldsymbol{k}')}$ ideal for a comprehensive instability saturation analysis.

On the right-hand side of Equation (3a), the second term is the nonlinear coupling between eigenmodes with $k_z' \neq 0$ and $k_z'' \neq 0$ (hence the two βs), and the third term, with an F and a β, is the nonlinear coupling between eigenmodes with $k_z' = 0$ and $k_z'' \neq 0$ (see the last paragraph of Section 2.1). Equations (3a) and (3b) have the same number of degrees of freedom as the original nonlinear equations in physical space, Equations (1a)–(1b). These systems are completely equivalent, but one represents dynamics in physical space and the other in eigenmode space.

3.2. Mode Energy Evolution

The energy evolution equation for each eigenmode can now be derived by multiplying Equation (3a) by β_j^* and adding the complex conjugate of the resulting equation, to arrive at

$$\partial_t |\beta_j|^2 = Q_j + T_{jAA}, \qquad (4)$$

where $Q_j = 2 \, \mathrm{Re} \, \gamma_j |\beta_j|^2$ is the linear energy transfer rate to $\boldsymbol{k}$ from the mean gradients, and T_{jAA} is the total nonlinear energy transfer to the jth eigenmode from *all* possible nonlinear interactions; Equation (C3). We now show the spectrum of time-averaged Q_1, along with that of the growth rate and time-averaged viscous dissipation rate ϵ_ν, in Figure 3.

From T_{jAA} in Equation (4), we separate out the nonlinear transfer $T_{1\mathcal{Z}1}$ in a triad that involves a latitudinal flow $\mathcal{Z}$ at
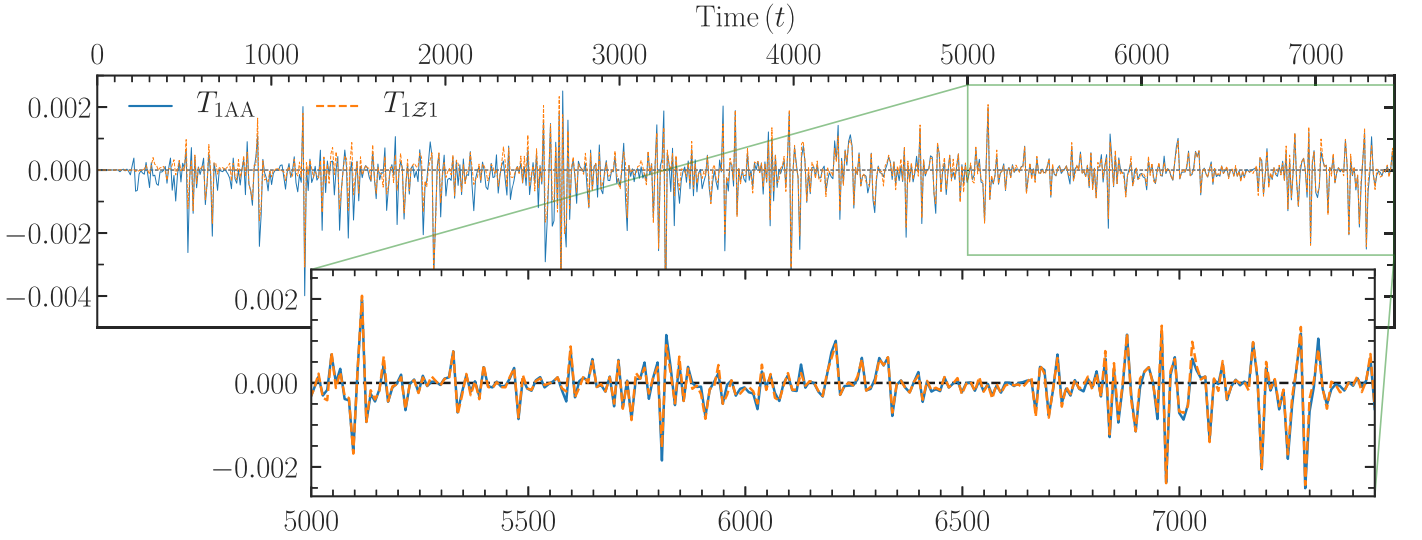
Figure 4. Time evolution of the total nonlinear energy transfer T_{1AA} to an unstable eigenmode at a wavenumber where the spectrum of $\langle \tilde{u}_x \tilde{u}_y \rangle$ peaks. $T_{1\mathcal{Z}1}$ is the energy transfer to the same unstable mode via interactions between the z-component of velocity ($\mathcal{Z}$) with wavenumbers $k_z = 0$ and to the other unstable modes. Comparison of the two transfer functions reveals that the dominant triad involves a latitudinal flow and two unstable modes. The simulation parameters are $S = 2.1$, $N^2 = 10$, and Pr = 0.01.

$k_z' = 0$ and two GSF-unstable modes ($j = 1$) at $k_z' \neq 0$:

$$T_{1\mathcal{Z}1} = \sum_{\mathbf{k}':k_z'=0} 2\,\mathrm{Re}\,\{[C_{1\mathcal{Z}1}^{(\mathbf{k},\mathbf{k}')} + C_{11\mathcal{Z}}^{(\mathbf{k},\mathbf{k}'')}]\mathcal{Z}'\beta_1''\beta_1^*\}. \quad (5)$$

We now compare $T_{1\mathcal{Z}1}$ with T_{1AA} in Figure 4, for a GSF-unstable mode with a wavenumber that contributes the most to the momentum transport. Repeating this transfer analysis at different wavenumbers produces similar results. The two transfers are nearly identical, which confirms the conjecture (Barker et al. 2019) that, in the fully nonlinear phase, the GSF instability saturates via the formation of strong latitudinal jets or flows. Such flows are z-directed, although with no z-variation, and primarily have a wavenumber $k_x = 2\pi/L_x$; see the right-column snapshot at $t = 6000$ in Figure 1. These flows generalize to meridional circulation in stars and resemble zonal jets in planetary atmospheres and fusion systems (Terry 2019). Flows with $k_z = 0$ are, however, linearly stable to the GSF instability, and thus must necessarily be excited nonlinearly by the interactions between the GSF-unstable modes. This energy received is then viscously damped at $k_z = 0$ and at low k_z, as seen in Figure 3. To sum up, the mean shear flow, destabilized by the thermal diffusion, lends energy to the fluctuations via the GSF-unstable modes, which saturate by exciting $k_z = 0$ latitudinal flows to a significant level. Such flows then viscously dissipate the turbulent energy. This is the saturation mechanism of the axisymmetric GSF instability found here.

4. AM Transport Model

The findings shown so far are sufficient to build a statistical closure model, with no free parameters, and thus with predictive power.

Equation (3a) has a quadratic nonlinearity, hence the evolutionary equations for mode energy contain triplet interactions (e.g., Equation (5)). To determine the evolving triplet interaction terms, one can derive an equation with quadruplet interactions (Equation (C6)), and so on. To truncate this never-ending hierarchy (the so-called "turbulence closure problem"), we invoke a standard turbulence closure, the Eddy-Damped Quasi-Normal Markovian (EDQNM) approximation

(see, e.g., Orszag 1970; Hegna et al. 2018; Terry et al. 2018, 2021; Li et al. 2021, 2023; Pueschel et al. 2021), which truncates the hierarchy at fourth-order cumulants of the fluctuations, thereby assuming that the statistics for the mode amplitudes are close to Gaussian. The resulting equation, however, is still nonlinear and daunting. But when a latitudinal flow $\mathcal{Z}$, with $k_z = 0$, dominates the nonlinear coupling, the complexity of the equation is significantly reduced (Terry et al. 2018).

4.1. An Outline of the Closure Model

We illustrate here the key steps involved in explaining most simply our closure model (by omitting details and treating all variables as real). First, we observe that Equation (3a) has the structure

$$\partial_t \beta = \dots \beta + \dots \beta\beta + \dots \beta\mathcal{X} + \dots \beta\mathcal{Y} + \dots \beta\mathcal{Z} + \dots \beta\Theta, \quad (6)$$

where the mode amplitudes are explicitly shown, and the dots (…) represent terms such as the linear growth rate and the nonlinear coupling coefficients. One can then obtain an evolution equation for the second-order correlator as $\partial_t(\beta\beta) = \dots \beta\beta + \dots \beta\mathcal{Z}\beta$, where the other nonlinear terms, e.g., $\beta\beta\beta$ and $\beta\beta\mathcal{X}$, have been dropped because the nonlinear energy transfer is almost entirely dominated by $\beta\mathcal{Z}\beta$—the latitudinal flow coupling (Figure 4). Since $\beta\mathcal{Z}\beta$ also evolves, one can similarly obtain an evolution equation for the third-order correlator as $\partial_t(\beta\mathcal{Z}\beta) = \dots \beta\mathcal{Z}\beta + \dots \beta\beta\mathcal{Z}\mathcal{Z}$. The closure solution then yields a relation $\beta\mathcal{Z}\beta = \dots \beta\beta\mathcal{Z}\mathcal{Z}$. Although useful later, this relation does not predict the mode amplitude β, needed for the turbulent transport prediction.

To predict the mode amplitude β, we consider the latitudinal flow evolution equation, $\partial_t \mathcal{Z} = \dots \mathcal{Z} + \dots \beta\beta$, and derive $\partial_t(\mathcal{Z}\mathcal{Z}) = \dots \mathcal{Z}\mathcal{Z} + \dots \beta\mathcal{Z}\beta$. Then, $\beta\mathcal{Z}\beta$ can be replaced with a product of four amplitudes, using the closure solution in the previous paragraph. One thus obtains $\partial_t(\mathcal{Z}\mathcal{Z}) = \dots \mathcal{Z}\mathcal{Z} + \dots \beta\beta\mathcal{Z}\mathcal{Z}$. In quasi-stationary turbulence, $\partial_t \sim 0$, and thus $\beta\beta\mathcal{Z}\mathcal{Z} = \dots \mathcal{Z}\mathcal{Z}$. The EDQNM closure allows us to write of a fourth-order correlator $\beta\beta\mathcal{Z}\mathcal{Z}$ as a sum of the products of the

second-order correlators, such as $|\beta|^2|\mathcal{Z}|^2$. Then, canceling $|\mathcal{Z}|^2$ from both sides of $\beta\beta\mathcal{Z}\mathcal{Z} = ... \mathcal{Z}\mathcal{Z}$, one predicts the saturated mode amplitude (or energy): $\beta\beta = ...$ Using this, one can make predictions for turbulent transport rates, as we shall show in the next subsection.

4.2. Detailed Closure Model

To make quantitative predictions for transport, we take the EDQNM-closed evolution equation for the latitudinal flow energy (see Appendix B, Equation (C13)):

$$\partial_t |\mathcal{Z}|^2 / 2 = -\gamma_{\mathcal{Z}} |\mathcal{Z}|^2 \\ + |\mathcal{Z}|^2 \sum_{\mathbf{k}'} |\beta_1'|^2 \, \text{Re} \, [-\tau_{11\mathcal{Z}} \overset{\leftrightarrow(\mathbf{k},\mathbf{k}')}{C_{\mathcal{Z}11}} \overset{\leftrightarrow(\mathbf{k}'',\mathbf{k})}{C_{1\mathcal{Z}1}}], \quad (7)$$

where, on the right-hand side, the second term contains a product of four amplitudes, but notably with $|\mathcal{Z}|^2$ that also appears in the first term of the right-hand side. In Equation (7),

$$\tau_{11\mathcal{Z}} = (\gamma_1' + \gamma_1'' - \gamma_{\mathcal{Z}}^*)^{-1}, \quad (8)$$

is the three-wave interaction time found from the EDQNM closure, and $\overset{\leftrightarrow(\mathbf{p},\mathbf{q})}{C_{lmn}} = C_{lmn}^{(\mathbf{p},\mathbf{q})} + C_{lnm}^{(\mathbf{p},\mathbf{p}-\mathbf{q})}$ is the symmetrized coupling coefficient. In quasi-stationary turbulence, $\partial_t \sim 0$, and thus the linear and nonlinear terms must balance. First, for simplicity, we consider a latitudinal flow at $(k_x, 0)$ that is driven by two unstable modes at (k_x', k_z') and $(k_x - k_x', -k_z')$; then, using Equation (7), $|\beta_1'|^2 = \gamma_{\mathcal{Z}} (\text{Re} \, [-\tau_{11\mathcal{Z}} \overset{\leftrightarrow(\mathbf{k},\mathbf{k}')}{C_{\mathcal{Z}11}} \overset{\leftrightarrow(\mathbf{k}'',\mathbf{k})}{C_{1\mathcal{Z}1}}])^{-1}$. A more general expression for $|\beta_1'|^2$ is found by using a standard Markovian assumption (Terry et al. 2021): $|\beta_1'|^2$ is more weakly dependent on wavenumbers than the other factors in Equation (7) arising from the coupling coefficients and $\tau_{11\mathcal{Z}}$. Such a consideration provides an expression for the nonlinearly saturated squared mode amplitude:

$$|\beta'|^2 = \gamma_{\mathcal{Z}} \times \left(\frac{\gamma}{k^2}\right)_{\text{Closure}}, \quad (9)$$

with

$$\left(\frac{\gamma}{k^2}\right)_{\text{Closure}} = \frac{1}{\left| \sum_{\mathbf{k}'} \tau_{11\mathcal{Z}} \, \text{Re} \, [-\overset{\leftrightarrow(\mathbf{k},\mathbf{k}')}{C_{\mathcal{Z}11}} \overset{\leftrightarrow(\mathbf{k}'',\mathbf{k})}{C_{1\mathcal{Z}1}}] \right|}, \quad (10)$$

where we note that the coupling coefficients scale linearly with wavenumbers, and $\tau_{11\mathcal{Z}}$ is the inverse of the sum of three growth rates of eigenmodes in a triad.

The growth rates in $\tau_{11\mathcal{Z}}$ should, in principle, also have amplitude-dependent eddy-damping rates as they become non-negligible, for example, in homogeneous isotropic fluid turbulence; however, when waves or instabilities exist, and when the turbulent transport spectrum is dominated by low wavenumbers, as in this study, $\tau_{11\mathcal{Z}}$ is approximated by using the linear growth rates (Terry et al. 2018, 2021). Using such, one identifies that the triplet interaction time $\tau_{11\mathcal{Z}}$ is maximal when the triad involves a latitudinal flow ($\mathcal{Z}$) and two GSF-unstable modes ($j = 1$). Shorter triplet interaction times $\tau_{12\mathcal{Z}}$ are expected for triads with, for example, the latitudinal flow, an unstable mode, and a strongly damped IGW ($j = 2$), as such an interaction lowers $\tau_{12\mathcal{Z}}$ via both the frequency and damping rate

of the IGW. The largest interaction time $\tau_{11\mathcal{Z}}$ dominates saturation.

The radial turbulent transport of AM is measured by $\langle \tilde{u}_x \tilde{u}_y \rangle \approx \sum_{\mathbf{k}'''} \hat{u}_{x,1}''' \hat{u}_{y,1}'''^* |\beta_1'''|^2$, where β_1''' is the unstable mode amplitude at $\mathbf{k}'''$ over which the summation is applied. Then, using $|\beta_1'''|^2$ from the above paragraph,

$$\langle \tilde{u}_x \tilde{u}_y \rangle_{\text{Closure}} = \left(\frac{\gamma}{k^2}\right)_{\text{Closure}} \times \gamma_{\mathcal{Z}} \sum_{\mathbf{k}'''} \hat{u}_{x,1}''' \hat{u}_{y,1}'''^*. \quad (11)$$

The y-component $\hat{u}_{y,1}'''$ of the velocity of the unstable eigenvector can be replaced with, e.g., its temperature perturbation $\hat{\theta}_1'''$ to predict the turbulent heat flux $\langle \tilde{u}_x \tilde{\theta} \rangle$.

In our simulations with radial differential rotation, the latitudinal momentum flux is much lower than the radial flux, and, when time-averaged, it is nearly null.

4.3. Tests of Theoretical Predictions

A simple quasi-linear (QL) model of the GSF instability saturation was recently proposed (Barker et al. 2019, 2020) by assuming that a secondary "parasitic" instability feeds on the primary GSF-unstable mode. Such an assumption, also called a "parasitic saturation mechanism" (Goodman & Xu 1994; Radko & Smith 2012; Brown et al. 2013; Harrington & Garaud 2019; Fraser et al. 2024), is based on a single primary mode at the fastest-growing wavenumber $\mathbf{k}'''$, which predicts the transport rate

$$\langle \tilde{u}_x \tilde{u}_y \rangle_{\text{QL}} = \frac{\gamma_1'''^2}{k_z'''^2} \hat{u}_{x,1}''' \hat{u}_{y,1}'''^* f^2(\mathbf{k}'''), \quad (12)$$

whose form is manifestly similar to Equation (11); the factor $f(\mathbf{k}''')$, which is evaluated at $\mathbf{k}''' = (0, k_z''')$, is the normalization factor of eigenmodes. Here, $\gamma_\nu''' = \gamma_1''' + \nu k'''^2$. To find $\langle \tilde{u}_x \tilde{\theta} \rangle_{\text{QL}}$, one can replace $\hat{u}_{y,1}'''$ on the right-hand side of Equation (12) with θ_1'''.

Predictions of Equations (11) and (12) are compared against the transport rates from direct numerical simulations in Figure 5. Significant improvements in both the momentum and heat transport predictions are observed with the statistical closure model. The orders-of-magnitude variation in transport rates is captured by the closure model.

In Figure 5, for smaller values of r, though the transport rates of the closure and the QL models are similar, we emphasize that this similarity is merely accidental: the two models incorporate very different physics. The assumptions of the closure model are supported by detailed numerical evidence (Figures 2 and 3), including the dominant three-wave coupling between two unstable modes and a latitudinal jet (Figure 4). No jet physics is considered in the QL model. The QL model predicts transport rates based on only one fastest-growing wavenumber k_z, with $k_x = 0$, which Figure 2 shows is inadequate. Hence, predictions of the QL model that tend to reproduce the data-validated closure model predictions are at best a fortuitous coincidence, occurring in a very limited parameter regime.

4.4. Impact of the New Model in Astrophysics

Since stellar interiors typically have extreme parameters, such as $\text{Pr} \lesssim 10^{-6}$, current and anticipated near-future computational resources are insufficient to permit direct numerical
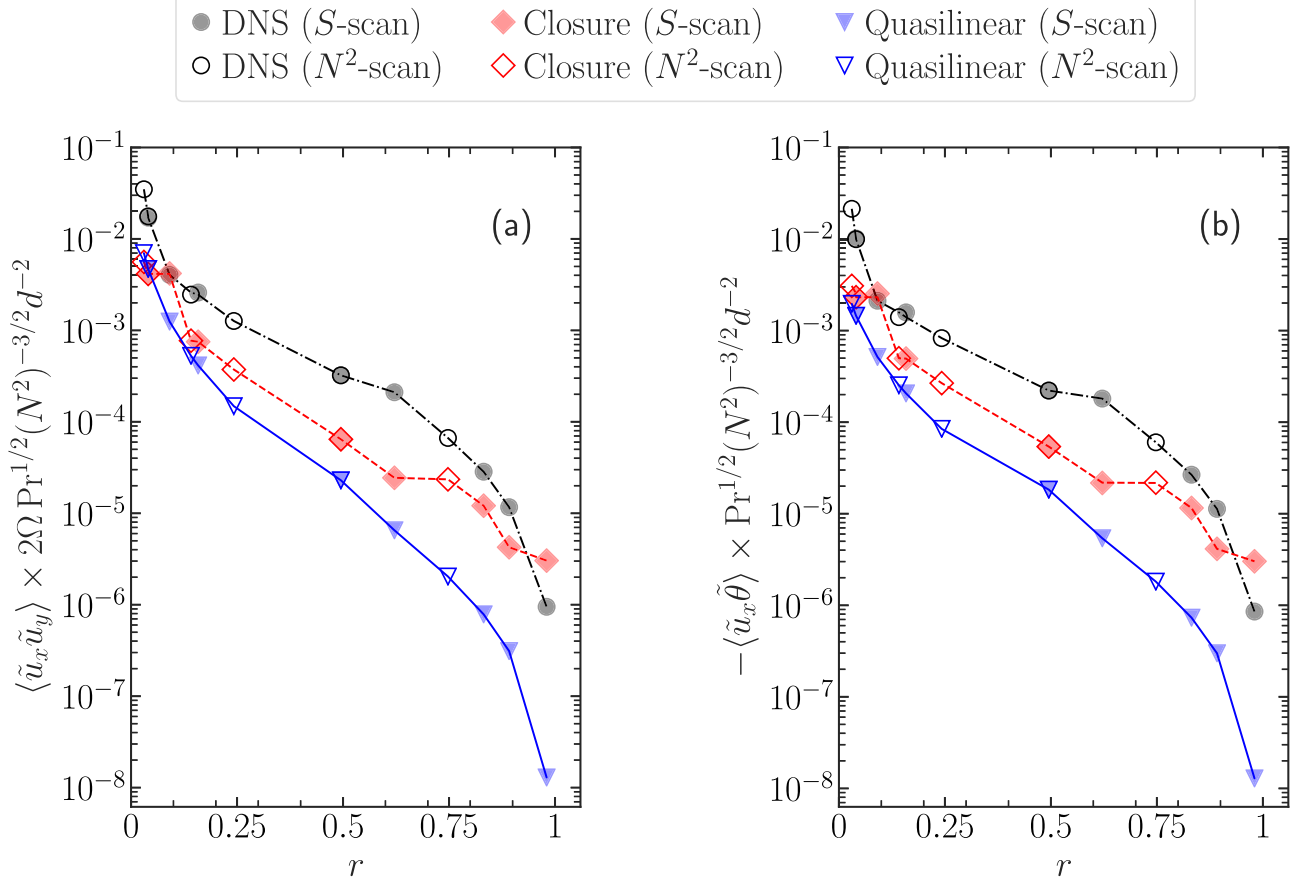
Figure 5. Tests of predictions of our closure model (red diamonds) and a QL-type, parasitic saturation model (blue inverted triangles) against direct numerical simulations (DNS; black/gray circles). (a) Variations of momentum transport rates: the filled markers correspond to the cases where the shear parameter S is varied ($N^2 = 10$), while the unfilled markers correspond to the cases where the squared Brunt–Väisälä frequency N^2 is varied ($S = 2.1$). Both S- and N^2-scan results collapse onto a single master curve when $\langle \tilde{u}_x \tilde{u}_y \rangle$ is scaled by a factor shown on the y-axis that transforms the governing equations of the GSF instability studied here to depend on only two dimensionless parameters (r, Pr). The GSF instability operates when $r \in [0, 1)$ and Pr < 1 (Pr = 0.01 is chosen). The y-axis shown is precisely an expression for the chemical transport rate for the thermohaline instability (see Equation (15a)). (b) Heat transport rates, displaying nearly identical trends (see Equation (15b) for the scaling factor). The closure prediction agrees with full DNS better than the QL prediction over the scanned range of parameters.

simulations of realistic turbulence in them. In the face of such a challenge, progress can be made by developing analytical theories, informed and tested by numerical simulations at more accessible parameters. Thus, we now employ our analytical theory to extrapolate and make predictions for realistic astrophysical parameters. To achieve this, we derive fully analytic expressions for all elements of the closure model, assuming that the coupling of two GSF-unstable modes with the latitudinal jet remains dominant; see Appendices A and B.

We then compare the predictions of the closure model with those of the QL model, over a wide range of parameters Pr ≈ $10^{-7} - 1$ and $r \approx 10^{-5} - 1$ in Figure 6. Noting that $N^2 = 2(S - 2)[1 + r(Pr^{-1} - 1)]$, these scans span $N^2 \lesssim 19 \times 10^6$ (in terms of Ω^2); this ratio is typically around 1 million for the Sun (Christensen-Dalsgaard et al. 1996). In Figure 6, with $S = 3$ (in terms of Ω), the Richardson number is as large as $\approx 2 \times 10^6$. More extreme parameters can be easily and quickly scanned with the analytic formula we have derived.

Now we predict the transport efficiency of the GSF instability in stars. The Reynolds stress is of order $\langle \tilde{u}_x \tilde{u}_y \rangle H^{-1}$, where $H \equiv U_0 (\partial_x U_0)^{-1}$ is the scale height of the mean flow $U_0 = -Sx$. The timescale for modifying the flow is $\tau_{\mathrm{turb}} \sim U_0 H / \langle \tilde{u}_x \tilde{u}_y \rangle \sim S x^2 \Omega^{-1} d^{-2} / \langle \tilde{u}_x \tilde{u}_y \rangle_{\mathrm{dimensionless}}$ (see also Barker et al. 2019).

Though Pr $\sim 10^{-6}$, the typical values of r in the solar tachocline and red giant stars are $r \sim 10^{-3} - 1$ (varying with radius). Then, using Figure 6, where $\langle \tilde{u}_x \tilde{u}_y \rangle_{\mathrm{dimensionless}}$ is on average 0.5, we predict $\tau_{\mathrm{turb}} \Omega \sim 2S(x/d)^2$. This turbulent transport timescale is sufficiently short to be astrophysically important, depending on the relative length scale x/d of the mean flow and shear strength S. For example, it can be as short as $\mathcal{O}(10)$ Myr using values of S and x/d for the solar tachocline.

The turbulent transport rate also depends sensitively on the shear parameter S (and latitude and orientation of the shear, i.e., radial or mixed radial–horizontal shear), and orders-of-magnitude faster turbulent transport is possible. We highlight that because the turbulent timescale for the GSF instability can be shorter than $\mathcal{O}(10)$ Myr, the incorporation of our transport model for the GSF turbulence in stellar evolution codes is warranted (particularly if extended to nonequatorial and 3D GSF instabilities). Using such, the long-term impact on the evolution of the rotation profile may be assessed, informing us of the effects of the GSF instability in rapidly rotating young stars. In this regard, the transport model built here for the 2.5D equatorial GSF instability (and the thermohaline instability) is significant, as a reliable and reduced numerical treatment of the GSF-instability-driven turbulence is now available.
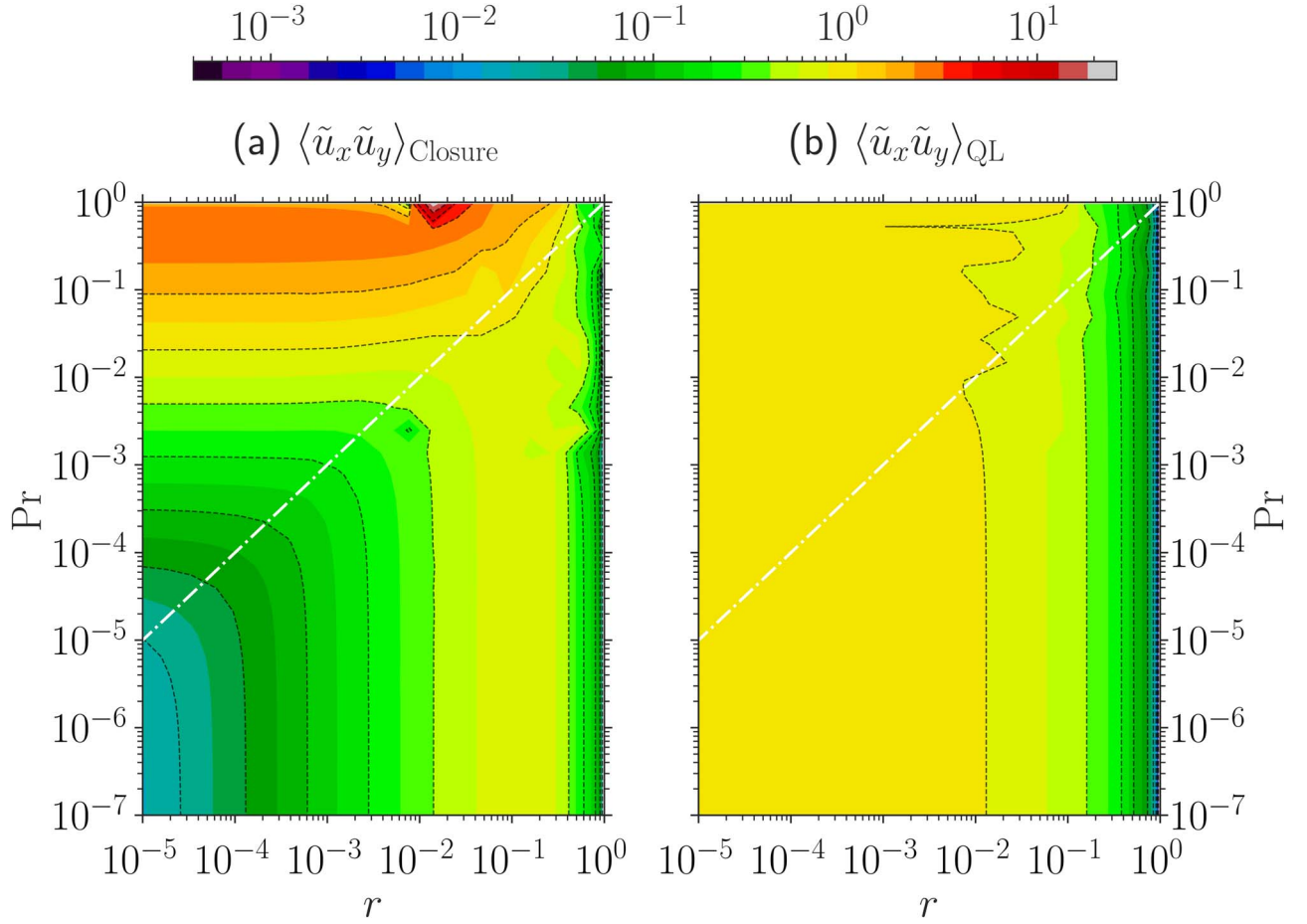
Figure 6. Predictions of (a) the closure model and (b) the QL model for turbulent momentum transport. The QL model, largely independent of Pr, fails to reproduce the behavior of the closure model. For Pr closer to 1, the closure model predicts the transport rate to increase with decreasing r—until an asymptotically large transport is attained. For Pr $\ll r$, the transport first increases and then decreases with r, in contrast to the QL prediction. The white dashed–dotted line, with a unit slope, separates the distinct regimes of Pr $< r$ and Pr $> r$ found in (a).

4.5. Relation to the Thermohaline Instability

We emphasize that the equations describing the 2.5D thermohaline and GSF instabilities at the equator are identical, when the compositional diffusivity is equal to the kinematic viscosity—a case often realized in stars. We first write Equations (7)–(9) of Brown et al. (2013), where they measure distance in units of the characteristic length scales d of the fingers, time in units of the characteristic diffusion timescale $\tau = d^2/\kappa$, and scaled temperature T in units of $N^2 d$ (we label their x-coordinate with our z-coordinate and vice versa):

$$\mathrm{Pr}^{-1} D u_x^{\mathrm{B}} = -\partial_x p^{\mathrm{B}} + (T^{\mathrm{B}} - \mu^{\mathrm{B}}) + \nabla^2 u_x^{\mathrm{B}}, \tag{13a}$$

$$\mathrm{Pr}^{-1} D u_z^{\mathrm{B}} = -\partial_z p^{\mathrm{B}} + \nabla^2 u_z^{\mathrm{B}}, \tag{13b}$$

$$D T^{\mathrm{B}} = -u_x^{\mathrm{B}} + \nabla^2 T^{\mathrm{B}}, \tag{13c}$$

$$D \mu^{\mathrm{B}} = -\frac{u_x^{\mathrm{B}}}{R_0} + \mathrm{Pr} \nabla^2 \mu^{\mathrm{B}}, \tag{13d}$$

where the state vector $[u_x^{\mathrm{B}}, u_z^{\mathrm{B}}, T^{\mathrm{B}}, \mu^{\mathrm{B}}, p^{\mathrm{B}}]$ represents Brown-normalized x- and z-velocities, scaled temperature, chemical concentration, and fluid pressure, respectively. The so-called density ratio $R_0 = -N^2/\kappa_{\mathrm{ep}}^2$ may be recast as $R_0 = 1 + r(\mathrm{Pr}^{-1} - 1)$. The solutions of Equations (13a)–(13d) critically depend only on two parameters: Pr and r. Equations (13a)–(13d) for the thermohaline instability with

the state vector $[u_x^{\mathrm{B}}, u_z^{\mathrm{B}}, T^{\mathrm{B}}, \mu^{\mathrm{B}}]$ are identical to Equations (1a) and (1b) for the GSF instability with the state vector $[u_x, u_z, \theta, u_y]$, when we note

$$u_x^{\mathrm{B}} = \frac{u_x}{d/\tau}, \tag{14a}$$

$$u_z^{\mathrm{B}} = \frac{u_z}{d/\tau}, \tag{14b}$$

$$T^{\mathrm{B}} = \frac{\theta}{N^2 d}, \tag{14c}$$

$$\mu^{\mathrm{B}} = -\frac{2\tau\Omega}{\mathrm{Pr}} \frac{u_y}{d/\tau}. \tag{14d}$$

Hence, the transport rates with two kinds of nondimensionalizations—one using τ and d as the characteristic timescale and length scale, and another using Ω and d as the relevant scales—are related in the manner

$$-\langle \tilde{u}_x^{\mathrm{B}} \tilde{\mu}^{\mathrm{B}} \rangle = \langle \tilde{u}_x \tilde{u}_y \rangle \times 2\Omega \mathrm{Pr}^{1/2} (N^2)^{-3/2} d^{-2}, \tag{15a}$$

$$\langle \tilde{u}_x^{\mathrm{B}} \tilde{T}^{\mathrm{B}} \rangle = \langle \tilde{u}_x \tilde{\theta} \rangle \times \mathrm{Pr}^{1/2} (N^2)^{-3/2} d^{-2}, \tag{15b}$$

where the variables with the superscripted "B" are functions of two essential parameters—r and Pr only, whereas the variables without the superscript are functions defined by the parameters Pr, S, and N^2.

The expressions given in Equations (15a) and (15b) are plotted in Figure 5. Thus, our Figure 5 also represents a comparison of the chemical and heat transport between direct numerical simulations and analytical models for the thermohaline-instability-driven turbulence.

The reduction of the governing equations of the GSF instability to two parameters (r, Pr) is realized only in the 2.5D equatorial case, which is where the analogy of the GSF instability with the thermohaline instability becomes exact.

5. Discussion and Conclusions

Turbulent transport in stellar interiors is a phenomenon too complex to be represented directly in stellar evolution models. It is often parameterized using low-order models, such as mixing-length theories, or models that predict transport rates based on the fastest-growing unstable mode (e.g., Denissenkov 2010; Brown et al. 2013; Barker et al. 2019). The reliability of such models can be compromised by several factors. First, the instability dispersion relation is often anisotropic, a property that affects the nonlinear energy transfer, thereby driving low-frequency fluctuations (Figure 3). Second, nonlinear mode coupling can strongly excite more weakly growing unstable modes over a wide range of wavenumbers, presenting difficulties to single-mode theory-based predictions. To circumvent such challenges, we build a nonlinear mode-coupling theory, informed by detailed analyses of direct numerical simulations, to arrive at a reliable and analytic transport model that is free of tunable parameters. We achieve this here for axisymmetric low-Pr turbulence driven by centrifugally unstable differential rotation (the GSF instability) at the equator in a stellar radiative zone.

Although 2.5D turbulence driven by the GSF instability can differ from fully 3D cases (Barker et al. 2019), strong secondary flows or jets have also been found in 3D global systems. For example, recent simulations of fully 3D spherical shell nonrotating fingering convection have exhibited strong, large-scale jets (Tassin et al. 2023). Such coherent jets are ubiquitous in various settings, such as in geo- and astrophysical observations, numerical simulations of 3D shear-flow-instability-driven turbulence (Tripathi et al. 2023b), and in laboratory fusion plasmas (Terry 2019). The examples show that large-scale flows can emerge even in global geometry. Hence, the success of our theory offers a future possibility for extending the statistical closure framework presented here to the more realistic 3D simulations of the GSF instability, ideally in a sphere, at a general latitude and for a range of Pr (Garaud & Brummell 2015; Barker et al. 2020; Dymott et al. 2023). It is also possible that our closure model framework can be adapted to magnetized turbulence driven by unstable differential rotation.

Since our formulae are fully analytic, they are quick to implement in stellar evolution codes such as MESA (Paxton et al. 2011, 2019) to reliably predict axisymmetric GSF-instability-driven turbulent transport rates that vary with Pr and r at different spatial grid points in an evolving star. It is straightforward to compute the values of r and Pr at a given spatial grid point in a modeled star and to simply look up transport rates by using our Figure 6(a) to prescribe the rates of transport of AM and heat; to access the lookup table of transport, see the Data Availability section. Since we have also provided formulae and frameworks for the turbulent transport of the axisymmetric GSF-analogous thermohaline instability, there now exists a reliable chemical transport model that

employs DNS-confirmed key elements of nonlinear saturation of the instability in stars.

Data Availability

The GitHub[8] and Zenodo doi:10.5281/zenodo.10808281 repositories host the data presented in Figure 6(a) and a Python script where the closure model is implemented. Other data used in this article will be shared on reasonable request to the corresponding authors.

Appendix A
Nonlinear Mode-coupling Coefficients of the GSF Instability

The jth eigenvector of the linear operator $\boldsymbol{L}$ of the GSF instability satisfies

$$\hat{u}_{z,j} = -\frac{k_x}{k_z}\hat{u}_{x,j}; \quad \hat{\theta}_j = -\frac{N^2}{\gamma_{\kappa,j}}\hat{u}_{x,j}; \quad \hat{u}_{y,j} = -\frac{2\Omega - S}{\gamma_{\nu,j}}\hat{u}_{x,j}, \quad \text{(A1)}$$

using which the matrix $\boldsymbol{E}$ of eigenvectors can be created and inverted, as mentioned in the penultimate paragraph of Section 2.1. To expedite analytic calculations, one may solve for the adjoint solutions $\boldsymbol{Y}_j$ of $\boldsymbol{L}$, which are the eigenvectors of $\boldsymbol{L}^\dagger$. Such adjoint solutions $\boldsymbol{Y}_j$ form a biorthogonal basis with the eigenvectors $\boldsymbol{X}_j$ of $\boldsymbol{L}$ (Fraser et al. 2021; Tripathi et al. 2022a, 2023a, 2023b). That is, $\langle \boldsymbol{Y}_m, \boldsymbol{X}_j \rangle = \boldsymbol{Y}_m^{T*}\boldsymbol{X}_j \propto \delta_{j,m}$, where T* is the transpose conjugation operation; see Appendix A of Tripathi et al. (2022b) for a general mathematical proof. It is known that both $\boldsymbol{L}$ and $\boldsymbol{L}^\dagger$ have the same eigenvalues. The expedient adjoint technique is equivalent to inverting the matrix $\boldsymbol{E}$ of size 4×4, and they deliver completely identical results, which we have verified. The jth adjoint solution satisfies

$$\hat{u}_{z,j} = 0; \quad \hat{\theta}_j = \frac{k_z^2}{k^2\gamma_{\kappa,j}}\hat{u}_{x,j}; \quad \hat{u}_{y,j} = \frac{2\Omega k_z^2}{k^2\gamma_{\nu,j}}\hat{u}_{x,j}. \quad \text{(A2)}$$

---

[8] https://github.com/BindeshTripathi/GSF_transport

Using such, we write the nonlinear mode-coupling coefficient between the two eigenmodes m at wavenumber $\boldsymbol{k}'$ and n at $\boldsymbol{k}''$, impacting the eigenmode j at $\boldsymbol{k}$, as

$$C_{jmn}^{(\boldsymbol{k},\boldsymbol{k}')} = \frac{\langle \boldsymbol{Y}_j(\boldsymbol{k}), \boldsymbol{N}(\boldsymbol{X}'_m, \boldsymbol{X}''_n)\rangle}{\langle \boldsymbol{Y}_j(\boldsymbol{k}), \boldsymbol{X}_j(\boldsymbol{k})\rangle}, \tag{A3}$$

where $\boldsymbol{N}(\boldsymbol{X}'_m, \boldsymbol{X}''_n)$ is the nonlinearity vector; for example, its θ-component is $-\boldsymbol{u}'_m \cdot \nabla \theta''_n$.

Following this procedure, we have distilled the analytic coupling coefficients for the GSF instability and provide below their final expressions:

$$\overset{\leftrightarrow(\boldsymbol{k},\boldsymbol{k}')}{C}_{\mathcal{Z}11} = \frac{i(k_x'^2 - k_x''^2)}{k_z' f' f''}, \tag{A4}$$

where f is the eigenmode normalization factor. With inverse dimensions of $\hat{u}_{x,j}$, suitable mode normalizations can be $f' = k'/\gamma'$ or $f' = k'^2 d/(\gamma'\gamma'_\nu \tau)$ or their variants, with $\tau = d^2/\kappa$ as the characteristic diffusion timescale. Equation (A4) is simple, as it represents the coupling between two unstable modes that drive the latitudinal flow $\mathcal{Z}$. The second coupling coefficient required in the closure model is

$$\overset{\leftrightarrow(\boldsymbol{k}'',\boldsymbol{k})}{C}_{1\mathcal{Z}1} = ik_z' \frac{\left[\frac{k''^2}{N^2 k_z''^2}\left(1 - \frac{2k_x k_x''}{k''^2}\right) + \frac{1}{R_0 \gamma'_\nu \gamma_\nu''} - \frac{1}{\gamma_\kappa' \gamma_\kappa''} \right] f''}{\left[\frac{k''^2}{N^2 k_z''^2} + \frac{1}{R_0 \gamma_\nu''^2} - \frac{1}{\gamma_\kappa''^2} \right] f'}. \tag{A5}$$

We note that the coupling coefficients depend only on wavenumbers, the input parameters, such as N^2, Pr, and $R_0 = -N^2/\kappa_{\text{ep}}^2$, and the growth rates; the growth rates in turn depend only on wavenumbers and the input parameters (Equation (2)). Asymptotic approximation to the growth rate in the limit of, e.g., small Pr is possible (Brown et al. 2013).

Appendix B
Nonlinear Mode-coupling Coefficients of the Thermohaline Instability

Here we provide the analytic expressions needed for the closure model applicable to the thermohaline instability.

We find the jth eigenvector of the linear operator $\boldsymbol{L}$ found from Equations (13a)–(13d) for the thermohaline instability satisfies

$$\hat{u}_{z,j}^{\text{B}} = -\frac{k_x}{k_z}\hat{u}_{x,j}^{\text{B}}; \quad \hat{T}_j^{\text{B}} = -\frac{1}{\gamma_{\kappa,j}}\hat{u}_{x,j}^{\text{B}}; \quad \hat{\mu}_j^{\text{B}} = -\frac{1}{R_0 \gamma_{\nu,j}}\hat{u}_{x,j}^{\text{B}}. \tag{B1}$$

The jth adjoint solution for the thermohaline instability is

$$\hat{u}_{z,j}^{\text{B}} = 0; \quad \hat{T}_j^{\text{B}} = \frac{k_z^2 \text{Pr}}{k^2 \gamma_{\kappa,j}}\hat{u}_{x,j}^{\text{B}}; \quad \hat{\mu}_j^{\text{B}} = -\frac{k_z^2 \text{Pr}}{k^2 \gamma_{\nu,j}}\hat{u}_{x,j}^{\text{B}}. \tag{B2}$$

The coupling coefficients for the thermohaline instability are identically the same as those for the GSF instability; Equations (A4) and (A5) require only a minute modification: N^2 appearing twice in Equation (A5) should be replaced with Pr. We conclude that our closure model and predictions are directly applicable to the thermohaline instability as well. This is significant, because the turbulent transport efficiencies of these two instabilities in stars are not known, but are generally

thought to be important. With the closure model at hand, we can now make predictions reliably for both instabilities.

Appendix C
Details of Closure Model Calculations

To make the statistical closure model more accessible to a wide range of readers, we provide below detailed, step-by-step derivations.

C.1. Amplitude Evolution Equation

The mode amplitude β_j evolution equation, given in Equation (3a), for a wavenumber $\boldsymbol{k} = (k_x, k_z \neq 0)$, with $j = 1$, 2, or 3, is

$$\begin{aligned}
\partial_t \beta_j = {} & \gamma_j \beta_j + \sum_{\boldsymbol{k}',m,n} C_{jmn}^{(\boldsymbol{k},\boldsymbol{k}')}\beta'_m \beta''_n \\
& + \sum_{\boldsymbol{k}',n}\{[C_{j\mathcal{Y}n}^{(\boldsymbol{k},\boldsymbol{k}')} + C_{jn\mathcal{Y}}^{(\boldsymbol{k},\boldsymbol{k}'')}]\mathcal{Y}'\beta''_n \\
& + [C_{j\mathcal{Z}n}^{(\boldsymbol{k},\boldsymbol{k}')} + C_{jn\mathcal{Z}}^{(\boldsymbol{k},\boldsymbol{k}'')}]\mathcal{Z}'\beta''_n \\
& + [C_{j\Theta n}^{(\boldsymbol{k},\boldsymbol{k}')} + C_{jn\Theta}^{(\boldsymbol{k},\boldsymbol{k}'')}]\Theta'\beta''_n\}, \tag{C1}
\end{aligned}$$

whereas, at $\boldsymbol{k} = (k_x, k_z = 0)$, one finds that the fluctuation amplitude evolves according to Equation (3b), which is expanded below:

$$\partial_t \mathcal{Y} = -\gamma_{\mathcal{Y}} \mathcal{Y} + \sum_{\boldsymbol{k}',m,n:k_z=0} C_{\mathcal{Y}mn}^{(\boldsymbol{k},\boldsymbol{k}')}\beta'_m \beta''_n, \tag{C2a}$$

$$\partial_t \mathcal{Z} = -\gamma_{\mathcal{Z}} \mathcal{Z} + \sum_{\boldsymbol{k}',m,n:k_z=0} C_{\mathcal{Z}mn}^{(\boldsymbol{k},\boldsymbol{k}')}\beta'_m \beta''_n, \tag{C2b}$$

$$\partial_t \Theta = -\gamma_{\Theta} \Theta + \sum_{\boldsymbol{k}',m,n:k_z=0} C_{\Theta mn}^{(\boldsymbol{k},\boldsymbol{k}')}\beta'_m \beta''_n, \tag{C2c}$$

where $\gamma_{\mathcal{Y}} = \gamma_{\mathcal{Z}} = \nu k^2$ and $\gamma_{\Theta} = \kappa k^2$ are the damping rates.

C.2. Eigenmode Energy Evolution

To derive an evolution equation for energy in the jth eigenmode at $\boldsymbol{k} = (k_x, k_z \neq 0)$, we multiply Equation (C1) with β_j^* and add a complex conjugate of the resulting equation to arrive at

$$\begin{aligned}
\partial_t |\beta_j|^2 = {} & 2\,\text{Re}\,\gamma_j |\beta_j|^2 + \sum_{\boldsymbol{k}',m,n} 2\,\text{Re}\,[C_{jmn}^{(\boldsymbol{k},\boldsymbol{k}')}\langle \beta'_m \beta''_n \beta_j^*\rangle] \\
& + \sum_{\boldsymbol{k}'} 2\,\text{Re}\,\{[C_{j\mathcal{Y}j}^{(\boldsymbol{k},\boldsymbol{k}')}\langle \mathcal{Y}\beta''_j \beta_j^*\rangle \\
& + C_{j\mathcal{Z}j}^{(\boldsymbol{k},\boldsymbol{k}')}\langle \mathcal{Z}'\beta''_j \beta_j^*\rangle + C_{j\Theta j}^{(\boldsymbol{k},\boldsymbol{k}')}\langle \Theta'\beta''_j \beta_j^*\rangle]|_{k_z'=0} \\
& + [C_{jj\mathcal{Y}}^{(\boldsymbol{k},\boldsymbol{k}')}\langle \beta'_j \mathcal{Y}''\beta_j^*\rangle + C_{jj\mathcal{Z}}^{(\boldsymbol{k},\boldsymbol{k}')}\langle \beta'_j \mathcal{Z}''\beta_j^*\rangle \\
& + C_{jj\Theta}^{(\boldsymbol{k},\boldsymbol{k}')}\langle \beta'_j \Theta''\beta_j^*\rangle]|_{k_z'=k_z}\}. \tag{C3}
\end{aligned}$$

Similar equations can be derived for the fluctuation energy at GSF-stable wavenumbers $\boldsymbol{k} = (k_x, k_z = 0)$ using Equations (C2a)–(C2c):

$$\begin{aligned}
\partial_t |\mathcal{Y}|^2 = {} & -2\,\text{Re}\,\gamma_{\mathcal{Y}} |\mathcal{Y}|^2 + \sum_{\boldsymbol{k}',m} 2\,\text{Re} \\
& \times [C_{\mathcal{Y}mm}^{(\boldsymbol{k},\boldsymbol{k}')}\langle \beta'_m \beta''_m \mathcal{Y}^*\rangle]|_{k_z=0}, \tag{C4a}
\end{aligned}$$

$$\partial_t |\mathcal{Z}|^2 = -2\,\mathrm{Re}\,\gamma_\mathcal{Z}|\mathcal{Z}|^2 + \sum_{k',m} 2\,\mathrm{Re}$$
$$\times\, [C^{(k,k')}_{\mathcal{Z}mm}\langle \beta'_m \beta''_m \mathcal{Z}^*\rangle]|_{k_z=0}, \tag{C4b}$$

$$\partial_t |\Theta|^2 = -2\,\mathrm{Re}\,\gamma_\Theta|\Theta|^2 + \sum_{k',m} 2\,\mathrm{Re}$$
$$\times\, [C^{(k,k')}_{\Theta mm}\langle \beta'_m \beta''_m \Theta^*\rangle]|_{k_z=0}. \tag{C4c}$$

Since numerical simulations inform us that the triplets with a latitudinal flow at $(k_x, 0)$, i.e., $\mathcal{Z}$, dominate the nonlinear energy transfer, we may drop nonlinear terms on the right-hand side of Equation (C3) that do not involve $\mathcal{Z}$. In the resulting equation, because $\mathcal{Y}$ and Θ do not appear, Equations (C4a) and (C4c) can also be removed, which allows us to write the following set of equations:

$$\partial_t |\beta_j|^2 = 2\,\mathrm{Re}\,\gamma_j |\beta_j|^2 + \sum_{k'} 2\,\mathrm{Re}\,\{[C^{(k,k')}_{j\mathcal{Z}j}\langle \mathcal{Z}'\beta''_j \beta^*_j\rangle]|_{k'_z=0}$$
$$+\, [C^{(k,k')}_{jj\mathcal{Z}}\langle \beta'_j \mathcal{Z}''\beta^*_j\rangle]|_{k'_z=k_z}\}, \tag{C5a}$$

$$\partial_t |\mathcal{Z}|^2 = -2\,\mathrm{Re}\,\gamma_\mathcal{Z}|\mathcal{Z}|^2$$
$$+ \sum_{k',m} 2\,\mathrm{Re}\,[C^{(k,k')}_{\mathcal{Z}mm}\langle \beta'_m \beta''_m \mathcal{Z}^*\rangle]|_{k_z=0}. \tag{C5b}$$

C.3. Triplet Correlation Evolution

To obtain evolution equations for the terms on the right-hand side of Equations (C5a) and (C5b), we multiply Equation (3a) with two amplitudes. For example, to determine the evolution of $\langle \mathcal{Z}'\beta''_j \beta^*_j\rangle$, we first multiply Equation (C1) for β_j with $\mathcal{Z}'\beta''_j$; second, we multiply another equation, similar to Equation (C1), but for β''_j with $\mathcal{Z}'\beta^*_j$; and finally, we multiply Equation (C2b), for $\mathcal{Z}'$, with $\beta''_j \beta^*_j$, and add them all together. Using this, we provide below an example evolution equation for triplet correlations:

$$[\partial_t - (-\gamma'_\mathcal{Z} + \gamma''_j + \gamma^*_j)]\langle \mathcal{Z}'\beta''_j \beta^*_j\rangle|_{k'_z=0}$$
$$=\Big\{\sum_{k''',m}[C^{(k',k''')}_{\mathcal{Z}mm}\langle \beta'''_m \beta_m(k'-k''')\beta''_j \beta^*_j\rangle]$$
$$+ \sum_{k'''_x}[C^{(k-k',k''')}_{j\mathcal{Y}j}\langle \mathcal{Y}'''\beta_j(k-k'-k''')\mathcal{Z}'\beta^*_j\rangle|_{k'''_z=0}$$
$$+ C^{(k-k',k''')}_{j\mathcal{Z}j}\langle \mathcal{Z}'''\beta_j(k-k'-k''')\mathcal{Z}'\beta^*_j\rangle|_{k'''_z=0}$$
$$+ C^{(k-k',k''')}_{j\Theta j}\langle \Theta'''\beta_j(k-k'-k''')\mathcal{Z}'\beta^*_j\rangle|_{k'''_z=0}$$
$$+ C^{(k-k',k''')}_{jj\mathcal{Y}}\langle \beta'''_j \mathcal{Y}(k-k'-k''')\mathcal{Z}'\beta^*_j\rangle|_{k'''_z=k_z}$$
$$+ C^{(k-k',k''')}_{jj\mathcal{Z}}\langle \beta'''_j \mathcal{Z}(k-k'-k''')\mathcal{Z}'\beta^*_j\rangle|_{k'''_z=k_z}$$
$$+ C^{(k-k',k''')}_{jj\Theta}\langle \beta'''_j \Theta(k-k'-k''')\mathcal{Z}'\beta^*_j\rangle|_{k'''_z=k_z}]$$
$$+ \sum_{k'''_x}[C^{(k,k''')*}_{j\mathcal{Y}j}\langle \mathcal{Y}'''*\beta^*_j(k-k''')\mathcal{Z}'\beta''_j\rangle|_{k'''_z=0}$$
$$+ C^{(k,k''')*}_{j\mathcal{Z}j}\langle \mathcal{Z}'''*\beta^*_j(k-k''')\mathcal{Z}'\beta''_j\rangle|_{k'''_z=0}$$
$$+ C^{(k,k''')*}_{j\Theta j}\langle \Theta'''*\beta^*_j(k-k''')\mathcal{Z}'\beta''_j\rangle|_{k'''_z=0}$$
$$+ C^{(k,k''')*}_{jj\mathcal{Y}}\langle \beta'''_j*\mathcal{Y}^*(k-k''')\mathcal{Z}'\beta''_j\rangle|_{k'''_z=k_z}$$
$$+ C^{(k,k''')*}_{jj\mathcal{Z}}\langle \beta'''_j*\mathcal{Z}^*(k-k''')\mathcal{Z}'\beta''_j\rangle|_{k'''_z=k_z}$$
$$+ C^{(k,k''')*}_{jj\Theta}\langle \beta'''_j*\Theta^*(k-k''')\mathcal{Z}'\beta''_j\rangle|_{k'''_z=k_z}]\Big\}|_{k'_z=0}. \tag{C6}$$

Since the numerical simulations show dominant coupling between the latitudinal flow $\mathcal{Z}$ and two unstable modes in a bath of turbulent interactions, the interactions involving unstable modes only can be excluded. This immediately implies that the first term on the right-hand side of Equation (C6) can be dropped in the face of the remaining dominant terms. Among the remaining terms, the fourth-order correlations that have different components of velocity, e.g., the terms where $\mathcal{Y}$ and $\mathcal{Z}$ appear together on the right-hand side of Equation (C6), do not form terms that appear in the definition of energy. Guided by numerical simulations where nonlinear coupling to $\mathcal{Y}$ and Θ are unimportant, only the energy(-like) terms with $\mathcal{Z}$ will be kept henceforth. The resulting equation then reads

$$[\partial_t - (-\gamma'_\mathcal{Z} + \gamma''_j + \gamma^*_j)]\langle \mathcal{Z}'\beta''_j \beta^*_j\rangle|_{k'_z=0}$$
$$=\Big\{\sum_{k'''_x}[C^{(k-k',k''')}_{j\mathcal{Z}j}\langle \mathcal{Z}'''\beta_j(k-k'-k''')\mathcal{Z}'\beta^*_j\rangle|_{k'''_z=0}$$
$$+ C^{(k-k',k''')}_{jj\mathcal{Z}}\langle \beta'''_j \mathcal{Z}(k-k'-k''')\mathcal{Z}'\beta^*_j\rangle|_{k'''_z=k_z}$$
$$+ C^{(k,k''')*}_{j\mathcal{Z}j}\langle \mathcal{Z}'''*\beta^*_j(k-k''')\mathcal{Z}'\beta''_j\rangle|_{k'''_z=0}$$
$$+ C^{(k,k''')*}_{jj\mathcal{Z}}\langle \beta'''_j*\mathcal{Z}^*(k-k''')\mathcal{Z}'\beta''_j\rangle|_{k'''_z=k_z}]\Big\}|_{k'_z=0}. \tag{C7}$$

The same procedure is then repeated to find evolution equations for the other two triplet correlations that appear in Equations (C5a) and (C5b).

C.4. Quadruplet Correlations and Statistical Closure Approximation

Equation (C7) can be solved using the technique of Green's function inversion and Markovianization, a standard step in EDQNM closure (although here we do not modify the growth rate γs with the amplitude-dependent nonlinear frequency, an approximation justifiable for the low-wavenumber regime; for more details, see Terry et al. 2018). Such a solution yields

$$\langle \mathcal{Z}'\beta''_j \beta^*_j\rangle|_{k'_z=0}$$
$$= -\{(-\gamma'_\mathcal{Z} + \gamma''_j + \gamma^*_j)^{-1}|\mathcal{Z}'|^2[(C^{(k'',-k')}_{j\mathcal{Z}j} + C^{(k'',k)}_{jj\mathcal{Z}})|\beta_j|^2$$
$$+ (C^{(k,k')*}_{j\mathcal{Z}j} + C^{(k,k'')*}_{jj\mathcal{Z}})|\beta''_j|^2]\}|_{k'_z=0}. \tag{C8}$$

Similarly, the other two triplet correlations that appear in Equations (C5a) and (C5b) can also be solved to obtain

$$\langle \beta'_j \mathcal{Z}''\beta^*_j\rangle|_{k'_z=k_z}$$
$$= -\{(\gamma'_j - \gamma_\mathcal{Z}'' + \gamma^*_j)^{-1}|\mathcal{Z}''|^2[(C^{(k',-k'')}_{j\mathcal{Z}j} + C^{(k',k)}_{jj\mathcal{Z}})|\beta_j|^2$$
$$+ (C^{(k,k'')*}_{j\mathcal{Z}j} + C^{(k,k')*}_{jj\mathcal{Z}})|\beta'_j|^2]\}|_{k'_z=k_z}, \tag{C9}$$

and

$$\langle \beta'_j \beta''_j \mathcal{Z}^*\rangle|_{k_z=0}$$
$$= -x\{(\gamma'_j + \gamma''_j - \gamma^*_\mathcal{Z})^{-1}|\mathcal{Z}|^2[(C^{(k',k)}_{j\mathcal{Z}j} + C^{(k',-k'')}_{jj\mathcal{Z}})|\beta''_j|^2$$
$$+ (C^{(k'',k)}_{j\mathcal{Z}j} + C^{(k'',-k')}_{jj\mathcal{Z}})|\beta'_j|^2]\}|_{k_z=0}. \tag{C10}$$

C.5. A Set of EDQNM-closed Energy Evolution Equations

The solutions of the triplet correlations from Equations (C8)–(C10) are now substituted into Equations (C5a) and (C5b), which results in the following set of closed equations:

$$\partial_t |\beta_j|^2 = 2 \operatorname{Re} \gamma_j |\beta_j|^2 - \sum_{k'} 2 \operatorname{Re}$$

$$\times \left[\frac{C_{j\mathcal{Z}j}^{(k,k')} |\mathcal{Z}'|^2}{(-\gamma_{\mathcal{Z}}' + \gamma_j'' + \gamma_j^*)} \{ \overset{\leftrightarrow(k'',-k')}{C_{j\mathcal{Z}j}} |\beta_j|^2 + \overset{\leftrightarrow(k,k')*}{C_{j\mathcal{Z}j}} |\beta_j''|^2 \} \right] \Bigg|_{k_z'=0}$$

$$- \sum_{k'} 2 \operatorname{Re} \left[\frac{C_{jj\mathcal{Z}}^{(k,k')} |\mathcal{Z}''|^2}{(\gamma_j' - \gamma_{\mathcal{Z}}'' + \gamma_j^*)} \right.$$

$$\times \{ \overset{\leftrightarrow(k',-k'')}{C_{j\mathcal{Z}j}} |\beta_j|^2 + \overset{\leftrightarrow(k,k'')*}{C_{j\mathcal{Z}j}} |\beta_j'|^2 \}] \Big|_{k_z'=k_z}, \tag{C11}$$

$$\partial_t |\mathcal{Z}|^2 = -2 \operatorname{Re} \gamma_{\mathcal{Z}} |\mathcal{Z}|^2 - |\mathcal{Z}|^2 \sum_{k'} \sum_{j=1}^{3} 2 \operatorname{Re}$$

$$\times \left[\frac{C_{\mathcal{Z}jj}^{(k,k')}}{(\gamma_j' + \gamma_j'' - \gamma_{\mathcal{Z}}^*)} \{ \overset{\leftrightarrow(k',k)}{C_{j\mathcal{Z}j}} |\beta_j''|^2 + \overset{\leftrightarrow(k'',k)}{C_{j\mathcal{Z}j}} |\beta_j'|^2 \} \right] \Bigg|_{k_z=0}, \tag{C12}$$

where $\overset{\leftrightarrow(p,q)}{C_{lmn}} = C_{lmn}^{(p,q)} + C_{lnm}^{(p,p-q)}$ is the symmetrized coupling coefficient.

Equation (C12) can be simplified by considering that it is the pairs of unstable modes ($j=1$) that excite the latitudinal flow $\mathcal{Z}$:

$$\partial_t |\mathcal{Z}|^2 / 2 = -\gamma_{\mathcal{Z}} |\mathcal{Z}|^2 + |\mathcal{Z}|^2 \sum_{k'} |\beta_1'|^2 \operatorname{Re}$$

$$\times \left[\frac{-\overset{\leftrightarrow(k,k')}{C_{\mathcal{Z}11}} \overset{\leftrightarrow(k'',k)}{C_{1\mathcal{Z}1}}}{\gamma_1' + \gamma_1'' - \gamma_{\mathcal{Z}}^*} \right], \tag{C13}$$

where the term inside the wavenumber summation in Equation (C12) has been symmetrized.

ORCID iDs

B. Tripathi ⓘ https://orcid.org/0000-0002-4723-2170
A. J. Barker ⓘ https://orcid.org/0000-0003-4397-7332
A. E. Fraser ⓘ https://orcid.org/0000-0003-4323-2082
P. W. Terry ⓘ https://orcid.org/0000-0002-4981-9637
E. G. Zweibel ⓘ https://orcid.org/0000-0003-4821-713X

References

Aerts, C., Mathis, S., & Rogers, T. M. 2019, ARA&A, 57, 35
Balbus, S. A., & Hawley, J. F. 1998, RvMP, 70, 1
Barker, A. J., Jones, C. A., & Tobias, S. M. 2019, MNRAS, 487, 1777
Barker, A. J., Jones, C. A., & Tobias, S. M. 2020, MNRAS, 495, 1468
Barker, A. J., & Latter, H. N. 2015, MNRAS, 450, 21
Beck, P. G., Montalban, J., Kallinger, T., et al. 2012, Natur, 481, 55

Biskamp, D., & Zeiler, A. 1995, PhRvL, 74, 706
Brown, J. M., Garaud, P., & Stellmach, S. 2013, ApJ, 768, 34
Christensen-Dalsgaard, J., Dappen, W., Ajukov, S. V., et al. 1996, Sci, 272, 1286
Denissenkov, P. A. 2010, ApJ, 723, 563
Du, S., Li, H., Fu, X., & Gan, Z. 2023, ApJ, 948, 72
Dymott, R. W., Barker, A. J., Jones, C. A., & Tobias, S. M. 2023, MNRAS, 524, 2857
Eggenberger, P., Montalbán, J., & Miglio, A. 2012, A&A, 544, L4
Fraser, A. E., Reifenstein, S. A., & Garaud, P. 2024, ApJ, 964, 184
Fraser, A. E., Terry, P. W., Zweibel, E. G., Pueschel, M. J., & Schroeder, J. M. 2021, PhPl, 28, 022309
Fricke, K. 1968, ZAp, 68, 317
Fuller, J., Piro, A. L., & Jermyn, A. S. 2019, MNRAS, 485, 3661
Garaud, P. 2018, AnRFM, 50, 275
Garaud, P., & Brummell, N. 2015, ApJ, 815, 42
Garaud, P., & Garaud, J. D. 2008, MNRAS, 391, 1239
Goldreich, P., & Schubert, G. 1967, ApJ, 150, 571
Goodman, J., & Xu, G. 1994, ApJ, 432, 213
Harrington, P. Z., & Garaud, P. 2019, ApJL, 870, L5
Hegna, C. C., Terry, P. W., & Faber, B. J. 2018, PhPl, 25, 022511
Knobloch, E. 1982, GApFD, 22, 133
Knobloch, E., & Spruit, H. C. 1982, A&A, 113, 261
Korycansky, D. G. 1991, ApJ, 381, 515
Latter, H. N., & Papaloizou, J. 2018, MNRAS, 474, 3110
Lesur, G., Flock, M., Ercolano, B., et al. 2023, in ASP Conf. Ser. 534, Protostars and Planets VII, ed. S.-i. Inutsuka et al. (San Francisco, CA: ASP), 465
Lesur, G., & Longaretti, P. Y. 2005, A&A, 444, 25
Li, P.-Y., Pueschel, M. J., Terry, P. W., & Whelan, G. G. 2023, NucFu, 63, 026028
Li, P.-Y., Terry, P. W., Whelan, G. G., & Pueschel, M. J. 2021, PhPl, 28, 102507
Nelson, R. P., Gressel, O., & Umurhan, O. M. 2013, MNRAS, 435, 2610
Ng, C. S., & Bhattacharjee, A. 1996, ApJ, 465, 845
Orszag, S. A. 1970, JFM, 41, 363
Park, J., Prat, V., & Mathis, S. 2020, A&A, 635, A133
Park, J., Prat, V., Mathis, S., & Bugnet, L. 2021, A&A, 646, A64
Paxton, B., Bildsten, L., Dotter, A., et al. 2011, ApJS, 192, 3
Paxton, B., Smolec, R., Schwab, J., et al. 2019, ApJS, 243, 10
Pueschel, M. J., Li, P. Y., & Terry, P. W. 2021, NucFu, 61, 054003
Radko, T., & Smith, D. P. 2012, JFM, 692, 5
Rashid, F. Q., Jones, C. A., & Tobias, S. M. 2008, A&A, 488, 819
Riley, J. J., & Lelong, M.-P. 2000, AnRFM, 32, 613
Smith, L. M., & Waleffe, F. 1999, PhFl, 11, 1608
Spiegel, E. A., & Veronis, G. 1960, ApJ, 131, 442
Spruit, H. C. 2002, A&A, 381, 923
Tassin, T., Gastine, T., & Fournier, A. 2023, arXiv:2309.01602
Terry, P. W. 2004, PhRvL, 93, 235004
Terry, P. W. 2019, in Theory, ed. B. Galperin & P. L. Read (Cambridge: Cambridge Univ. Press), 181
Terry, P. W., Faber, B. J., Hegna, C. C., et al. 2018, PhPl, 25, 012308
Terry, P. W., Li, P. Y., Pueschel, M. J., & Whelan, G. G. 2021, PhRvL, 126, 025004
Tripathi, B., Fraser, A. E., Terry, P. W., Zweibel, E. G., & Pueschel, M. J. 2022a, PhPl, 29, 070701
Tripathi, B., Fraser, A. E., Terry, P. W., Zweibel, E. G., & Pueschel, M. J. 2022b, PhPl, 29, 092301
Tripathi, B., Fraser, A. E., Terry, P. W., et al. 2023a, PhPl, 30, 072107
Tripathi, B., Terry, P. W., Fraser, A. E., Zweibel, E. G., & Pueschel, M. J. 2023b, PhFl, 35, 105151
Urpin, V., & Brandenburg, A. 1998, MNRAS, 294, 399
Waleffe, F. 1993, PhFlA, 5, 677
Wood, T. S., & McIntyre, M. E. 2011, JFM, 677, 445